Experimental and theoretical evidence for hydrogen doping in polymer solution-processed indium gallium oxide

Wei Huang[a,b], Po-Hsiu Chien[c,d], Kyle McMillen[e], Sawankumar Patel[c], Joshua Tedesco[f], Li Zeng[g,h], Subhrangsu Mukherjee[i], Binghao Wang[a,b], Yao Chen[a,b], Gang Wang[a,b], Yang Wang[a,b], Yanshan Gao[a,b], Michael J. Bedzyk[g,h,1], Dean M. DeLongchamp[i,1], Yan-Yan Hu[c,d,1], Julia E. Medvedeva[e,1], Tobin J. Marks[a,b,1], and Antonio Facchetti[a,b,j,1]

[a]Department of Chemistry, Northwestern University, Evanston, IL 60208; [b]Materials Research Center, Northwestern University, Evanston, IL 60208; [c]Department of Chemistry and Biochemistry, Florida State University, Tallahassee, FL 32306; [d]Center of Interdisciplinary Magnetic Resonance, National High Magnetic Field Laboratory, Tallahassee, FL 32310; [e]Department of Physics, Missouri University of Science and Technology, Rolla, MO 65409; [f]Department of Materials Science and Engineering, Rutgers, The State University of New Jersey, Piscataway, NJ 08901; [g]Applied Physics Program, Northwestern University, Evanston, IL, 60208; [h]Department of Materials Science and Engineering, Northwestern University, Evanston, IL, 60208; [i]Materials Science and Engineering Division, National Institute of Standards and Technology, Gaithersburg, MD 20899; and [j]Flexterra Corporation, Skokie, IL 60077

The field-effect electron mobility of aqueous solution-processed indium gallium oxide (IGO) thin-film transistors (TFTs) is significantly enhanced by polyvinyl alcohol (PVA) addition to the precursor solution, a >70-fold increase to 7.9 cm^2/Vs. To understand the origin of this remarkable phenomenon, microstructure, electronic structure, and charge transport of IGO:PVA film are investigated by a battery of experimental and theoretical techniques, including In K-edge and Ga K-edge extended X-ray absorption fine structure (EXAFS); resonant soft X-ray scattering (R-SoXS); ultraviolet photoelectron spectroscopy (UPS); Fourier transform-infrared (FT-IR) spectroscopy; time-of-flight secondary-ion mass spectrometry (ToF-SIMS); composition-/processing-dependent TFT properties; high-resolution solid-state ^{1}H, ^{71}Ga, and ^{115}In NMR spectroscopy; and discrete Fourier transform (DFT) analysis with ab initio molecular dynamics (MD) liquid-quench simulations. The ^{71}Ga{^{1}H} rotational-echo double-resonance (REDOR) NMR and other data indicate that PVA achieves optimal H doping with a Ga⋯H distance of ~3.4 Å and conversion from six- to four-coordinate Ga, which together suppress deep trap defect localization. This reduces metal-oxide polyhedral distortion, thereby increasing the electron mobility. Hydroxyl polymer doping thus offers a pathway for efficient H doping in green solvent-processed metal oxide films and the promise of high-performance, ultra-stable metal oxide semiconductor electronics with simple binary compositions.

oxide semiconductor | indium gallium oxide | hydrogen doping | polymer incorporation | transistor

Amorphous metal oxide (MO) semiconductors are of great fundamental scientific and technological interest due to their large band gaps and high electron mobilities (1–4), making them promising candidates for next-generation transparent and flexible electronics (5–9). Among these materials, indium gallium zinc oxide (IGZO) is by far the most investigated and technologically relevant, providing mobilities of 10 to 100 cm^2/Vs and stable operation in both crystalline and amorphous phases (10–12). Ga plays a key role in IGZO as an "oxygen getter," due to a greater oxygen binding enthalpy than In (13, 14). Thus, the carrier concentration in IGZO can be manipulated and stabilized by adjusting the Ga concentration (15), with manufactured sputtered IGZO devices having a Ga content of more than 30 atomic percent (at. %) (In:Ga:Zn ~ 1:1:1) for optimal thin-film transistor (TFT) switching (16, 17). Nevertheless, while Ga incorporation is essential for stable IGZO TFT operation, it comes at the cost of lower In_2O_3 matrix mobility (13).

Recently, solution-processing/annealing below 300 °C (18–20) has emerged as a viable alternative to physical vapor deposition for the growth/patterning of MO electronics, offering reduced production costs and large-scale production by printing (21–24). However, the mobilities of 2 to 6 cm^2/Vs in IGZO TFTs processed/annealed at 300 °C are only achieved at a Ga content of less than 10 at. % (18, 19) due to incomplete precursor conversion to pure, densified IGZO films. Adding more Ga (>20 at. %) exacerbates these issues, increasing trap densities by suppressing oxygen vacancies (15), and yielding substantially decreased mobilities—typically <1 cm^2/Vs for processing at a temperature of 300 °C (25, 26). Thus, solution processing of high-performance, high-Ga-content IGZO TFTs, or compositionally simpler and, hence, technologically more desirable indium gallium oxide (IGO) TFTs, remains challenging and an impediment to manufacturing low-temperature solution-processed MO electronics.

Significance

Solution processing of high-performance, high-Ga-content IGZO thin-film transistors (TFTs)—or compositionally simpler and, hence, technologically more desirable indium gallium oxide (IGO) TFTs—remains challenging and an impediment to manufacturing low-temperature, solution-processed metal oxide electronics. Here, the performance of aqueous solution-processed IGO TFTs is greatly enhanced with polyvinyl alcohol in the precursor solution, yielding a >70-fold increase in electron mobility. By achieving optimal H doping and conversion from six- to four-coordinate Ga, PVA addition suppresses deep trap defect localization. This result not only offers a route to high-performance, ultra-stable metal oxide semiconductor electronics with simple binary compositions, but also provides powerful tools to probe H locations in amorphous metal oxides via a combination of experimental and theoretical approaches.

CHEMISTRY

Here, we report an approach to enhancing electron mobilities in amorphous IGO (a-IGO) to levels approaching those in sputtered IGZO TFTs. Specifically, adding a hydroxyl-rich polymer, polyvinyl alcohol (PVA), to IGO (In:Ga = 6:4 mol ratio) precursor solutions yields IGO TFTs with mobilities as high as 7.9 cm^2/Vs for films processed at 300 °C. The microstructure, electronic structure, doping effects, and charge transport of IGO:PVA films are characterized by a battery of techniques, including In K-edge and Ga K-edge extended X-ray absorption fine structure (EXAFS); high-resolution solid-state (SS) ^{1}H, ^{71}Ga, and ^{115}In NMR spectroscopy; resonant soft X-ray scattering (R-SoXS); ultraviolet photoelectron spectroscopy (UPS); Fourier transform-infrared (FT-IR) spectroscopy; time-of-flight secondary-ion mass spectrometry (ToF-SIMS); and composition-/processing-dependent TFT properties, in concert with discrete Fourier transform (DFT) analysis and ab initio molecular dynamics (MD) liquid-quench simulations. Together, these provide evidence for H doping and -OH bonding effects that enhance mobility and electron-trap delocalization and represent a strategy for doping solution-processed MO semiconductors as well as fundamental insights of the doping mechanism.

Results

IGO:PVA Film Growth and Characterization. Solutions of MO film precursors In(NO$_3$)$_3$ and Ga(NO$_3$)$_3$ in deionized (DI) water, having x wt. % (used hereafter to denote mass %) PVA vs. IGO (x = 0 to 14), were spin-coated onto cleaned substrates and annealed at 300 °C for 30 min. This process was repeated three times to achieve film thicknesses of ~10 nm. PVA was chosen due to its solubility in the aqueous precursor solutions, high OH group content, and low acidity. All films are ultrasmooth with r.m.s. roughness (σ_{RMS}) ≤ 0.19 nm by atomic force microscopy (AFM) (Fig. 1A), are completely amorphous by grazing incidence X-ray diffraction (GIXRD) (Fig. 1B), and exhibit relatively large M–O–M lattice content (>70% for <12 wt. % PVA) by X-ray photoelectron spectroscopy (XPS) (Fig. 1C). Moreover, the carbon content of the IGO:PVA films measured by using XPS never exceeds 4.0 at. % (Fig. 1D). See *SI Appendix*, Figs. S1–S9 and Tables S1–S3 for AFM, GIXRD, and XPS data. These results indicate that much of the PVA is thermolyzed during annealing, and all IGO:PVA films have relatively large M–O–M lattice content, offering the potential to form high-performance MO TFTs with a high degree of uniformity over large areas.

IGO:PVA TFT Characteristics. To probe the electronic effects of PVA addition on IGO films, bottom-gate, top-contact IGO:PVA TFTs were characterized (see *Materials and Methods* for fabrication details). As shown in Fig. 2A, the IGO:PVA TFT transfer curves strongly depend on the PVA content, with tremendous on-current (I_{ON}; drain current measured at $V_{DS} = V_{GS} = +80$ V) and turn-on voltage (V_{ON}) variations. I_{ON} and V_{ON} data extracted from the forward-transfer curves are summarized in Fig. 2B. Neat IGO TFTs have low I_{ON} values (6.62 ± 2.23 × 10^{-7} A) and large positive V_{ON} values (+33.7 ± 12.3 V). With increasing PVA content from 0 to 8 wt. %, I_{ON} gradually rises (V_{ON} falls) to 1.25 ± 0.10 × 10^{-3} A (to −6.2 ± 2.1 V) for an 8 wt. % PVA loading, exhibiting >1,000x I_{ON} enhancement. Further addition of PVA to 14 wt. % depresses I_{ON} (increased V_{ON}) to 4.81 ± 0.31 × 10^{-5} A (to +38.1 ± 5.2 V). For all devices, I_{OFF} remains in the range of circa 10^{-10} A, indicating relatively low carrier concentrations, suitable for low-power-consumption TFTs. Furthermore, PVA addition strongly suppresses hysteresis ($\Delta V_{TH} < 2$ V with 8 wt. % PVA) vs. that in neat IGO TFTs, where $\Delta V_{TH} \sim 30$ V, indicating that optimal PVA addition substantially suppressed the trap density of IGO films and, hence, enhanced TFT performance.

The mobilities in saturation and V_T of IGO films were next extracted from the transfer plots (27), and data are shown in

Fig. 2C and *SI Appendix*, Table S4. While neat IGO TFTs have an electron mobility of 0.10 ± 0.04 cm^2/Vs, that in IGO:PVA TFTs maximized at 6.43 ± 0.73 cm^2/Vs for 8 wt. % PVA. To our knowledge, this is one of the highest reported values for high-Ga-content, solution-processed IGO films annealed at 300 °C or lower (see *SI Appendix*, Table S5 for comparisons to literature data). For larger PVA content, the mobility falls (1.25 ± 0.66 cm^2/Vs for 14 wt. % PVA), but remains higher than that in neat IGO. Similar to V_{ON}, V_T first falls from +36.4 ± 9.2 V (0 wt. % PVA) to +16.6 ± 2.7 V (8 wt. % PVA) and then rises to +50.4 ± 5.5 V (14 wt. % PVA). Low V_T in TFT is essential for low-power-consumption and low-driving-voltage applications (28). A lower processing temperature of 250 °C for IGO:PVA films was also investigated, and the performance enhancement of the corresponding TFTs is identical (*SI Appendix*, Fig. S10 and Table S6). Thus, optimization of the process as well as exploring other polymers may reduce the processing temperature even further. These TFT data indicate that PVA incorporation efficiently reduces electron charge-trap density in IGO and enhances mobility. This conclusion is supported by UPS and optical spectroscopic data (*SI Appendix*, Figs. S11–S13 and Table S7), which reveal that embedding PVA in IGO matrices lowered the work function (i.e., up-shifted the Fermi level).

IGO:PVA Film Microstructure. X-ray reflectometry (XRR) measurements were first carried out to analyze the microstructure of MO films as a function of PVA content. The average electron density and film thickness fall gradually from 1.42 e/Å^3 and 10.2 nm (0 wt. % PVA) to 1.30 e/Å^3 and 8.8 nm (14 wt. % PVA) (Fig. 3A and *SI Appendix*, Fig. S14 and Table S8). Next, EXAFS studies focused on atomistic microstructure details of IGO:PVA films and reveal few obvious absorption-profile variations with increasing PVA content in either the In K-edge and Ga K-edge data (Fig. 3B). Both coordination numbers (N) and bond lengths (R) of the first shell, along with the Debye–Waller factors, which measure structural disorder or variation, were computed and are summarized in *SI Appendix*, Fig. S15 and Table S9. The In–O and Ga–O coordination numbers remain in a narrow, undercoordinated range of 4.91 to 5.22 and 3.55 to 3.69, respectively, without obvious variations with PVA content. Similar evolutions
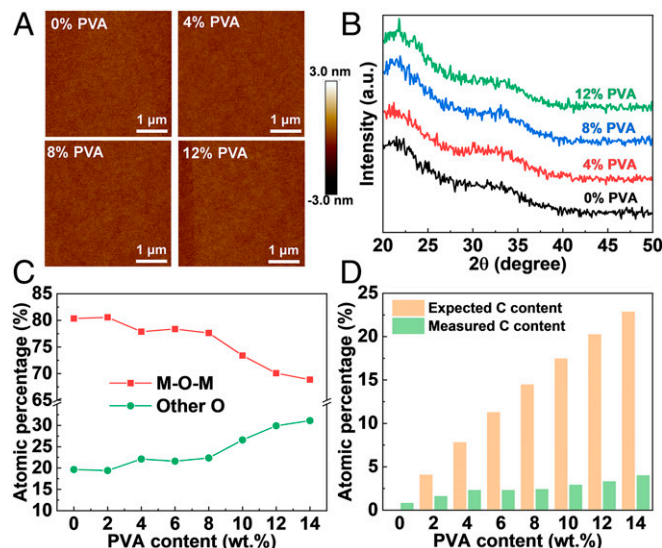
Fig. 1. Microstructure, composition, and morphology characterization of IGO:PVA films shown as a function of PVA content. (A) AFM images. (B) GIXRD 2θ scans. a.u., arbitrary units. (C) The O 1s XPS-derived M–O–M content vs. other oxygen species. (D) Theoretical vs. XPS-measured atomic C percentages.
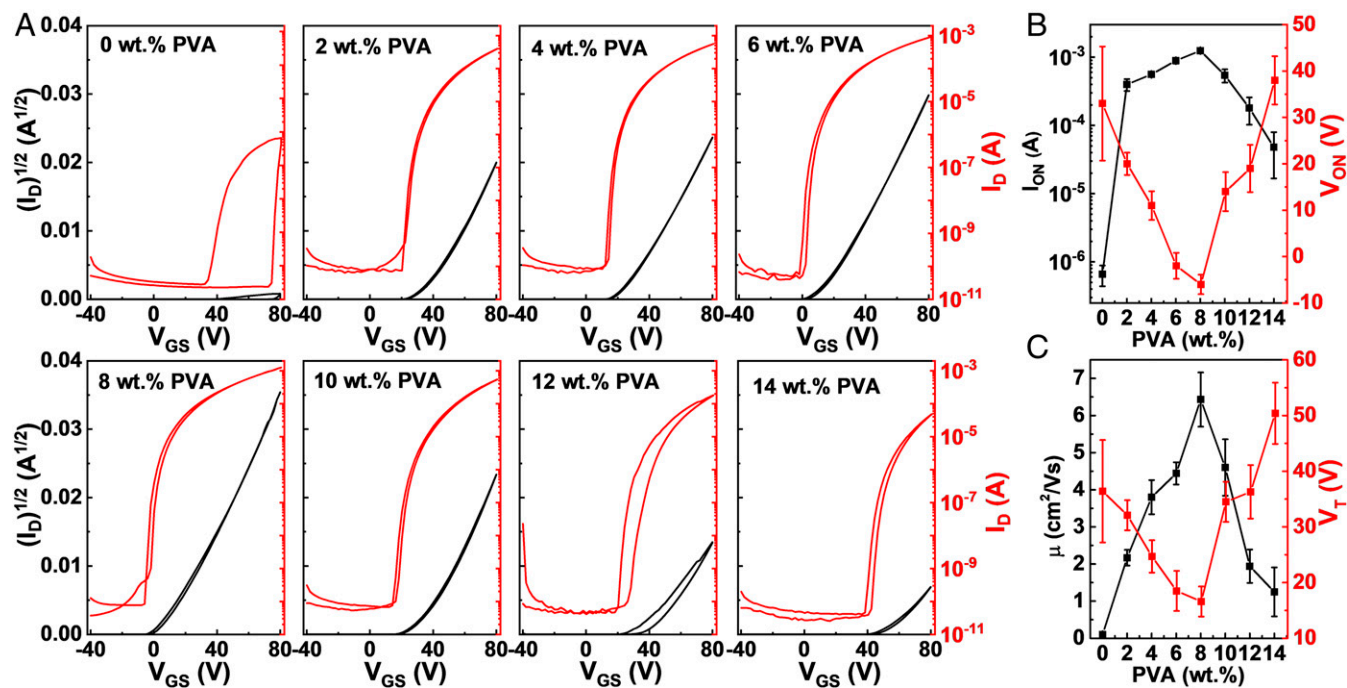
Fig. 2. IGO:PVA thin-film transistor characterization as a function of PVA content. (*A*) Representative transfer curves (V_{DS} = +80 V). (*B*) I_{ON} and V_{ON} variations. (*C*) Field-effect mobility and V_T of IGO:PVA TFTs. Each data point is an average of ≥10 devices.

are also found for the bond lengths, where the In–O first shell is 2.13 to 2.15 Å and that of the Ga–O first shell is 1.85 to 1.86 Å. While crystalline β-Ga_2O_3 has two close Ga–O distances of 1.85 Å (tetrahedral Ga) and 2.01 Å (octahedral Ga), only a single contact at ~1.85 Å is observed in IGO:PVA (15). Moreover, the first-shell Ga–O coordination number is ~3.6, indicating that most Ga ions occupy tetrahedral sites.

Next, R-SoXS was utilized to determine whether and to what extent phase separation accompanies PVA incorporation. As shown in Fig. 3*C*, in both neat IGO film and in IGO:PVA films with 8 wt. % PVA, no obvious change in profile shape is observed at off-resonant as well as near-resonant energies, while a peak at 30 to 40 nm is present in both films, suggesting little or no differences in in-plane morphology. The results further support the evidence that PVA significantly thermolyzes during the film fabrication and does not introduce phase separation in the resulting oxide films, which is beneficial for electron transport.

Since the above analyses do not provide conclusive information on how PVA enhances IGO:PVA transport properties, the question arises as to whether the smallest element, H, is involved. Several studies have investigated H incorporation in MO semiconductors such as ZnO and IGZO and suggested that H may act as a shallow donor by forming M–OH bonds or interstitial H⁻ sites (29–33). However, to the best of our knowledge, IGO has not been investigated. Various methods have been used to H-dope MO semiconductors (34–36), including wet-air annealing (37), H_2 annealing (38), and H plasma treatment (31, 38, 39), to cite just a few. For example, for pulsed laser deposition or sputtered MO films, residual H in the chamber is known to act as an H source (29, 30) and can dope MO films (40). However, the role of H is not unambiguous, as it may have multiple MO semiconductor states, with either weak/strong bonding or trap/donor-like states (38, 40). Moreover, in these previous studies, largely qualitative experiments established the presence of H, but the actual bonding character in semiconducting MO systems, especially in Ga-rich MO compositions, remains unclear, although calculations/simulations for crystalline In_2O_3 have suggested both substitutional and interstitial Hs (32, 41).

To quantify the nature and amount of H in the present IGO:PVA films, ToF-SIMS depth profiling and FT-IR spectroscopy were first applied to the IGO:PVA precursors and IGO:PVA films annealed at 300 °C, with careful experimental design. For ToF-SIMS depth-profile measurements, IGO:PVA films were grown identically to those for TFT fabrication, but using D_2O rather than H_2O as the solvent to understand the origin of the H in the IGO:PVA films. By monitoring the D concentration and D:H ratio in the ToF-SIMS depth profiling, no evidence of D incorporation is found in either the undoped films or films with 4 wt. %, 8 wt. %, and 12 wt. % PVA (42), even though NMR indicated rapid D/H exchange with PVA in solution (*SI Appendix*, Fig. S16). FT-IR spectra also reveal the absence of significant O–D stretching modes at ~2,600 cm^{-1}. Together, these results argue that the majority of H in the IGO films originates neither from the precursor solvent nor from the PVA, but, rather, from the ambient atmosphere during thermal precursor conversion to ~3-nm MO films and subsequent cooling in ambient with relative humidity = 30 to 50%. Additionally, the relative quantities of H vs. GaO_2 vs. OH (GaO_2 meaning the GaO_2^- ion peak) for H_2O-processed films were assessed by ToF-SIMS depth profiling (Fig. 3*D* and *SI Appendix*, Fig. S17). Note that the Si wafer–IGO:PVA film interface is clearly observed, indicating a relatively uniform etching process. Comparison of the H vs. GaO_2 and OH vs. GaO_2 molar ratios in Fig. 3*D* indicate that pristine IGO films (no PVA) have the highest H and OH concentrations (H/GaO_2 ~ 0.5; OH/GaO_2 ~ 6) compared to the IGO:PVA films. Note also that the H and OH content are lowest for 4 wt. % and 8 wt. % IGO:PVA (H/GaO_2 ~ 0.2; OH/GaO_2 ~ 2), with both ratios increasing slightly for 12 wt. % PVA (H/GaO_2 ~ 0.3; OH/GaO_2 ~ 3). The OH content in IGO:PVA films was further quantified by attenuated total reflection (ATR) FT-IR spectroscopy. As shown in Fig. 3*E*, on the bare SiO_2 substrates, O–H stretching modes are not evident, but only a very weak C–H stretching (~2,900 cm^{-1}), presumably from surface contamination. However, neat IGO films exhibit relatively strong O–H stretching mode(s) at 3,200 to 3,600 cm^{-1}, centered near ~3,470 cm^{-1}.
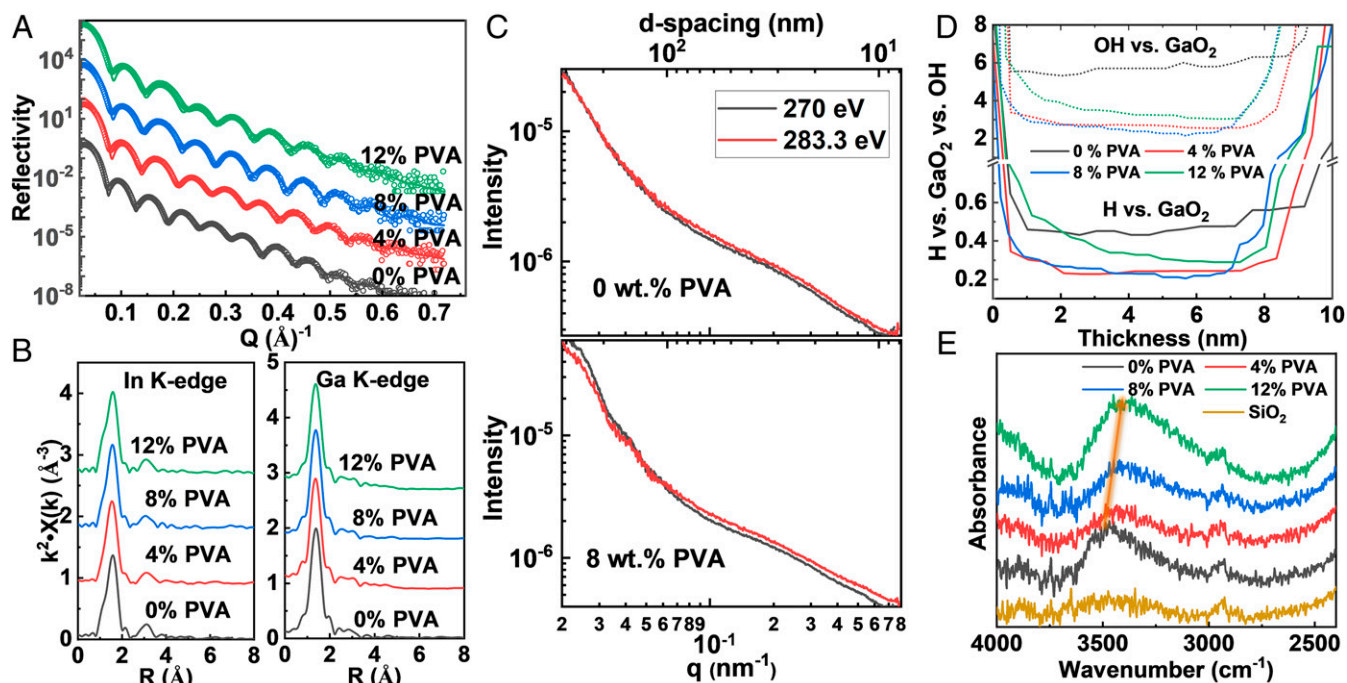
Fig. 3. (*A*) Representative XRR measurements (circles) and model fits (lines) of IGO:PVA films. (*B*) EXAFS measurements at the In K-edge and Ga K-edge. (*C*) R-SoXS of neat IGO and IGO with 8 wt. % PVA; film thickness is increased to ~40 nm to increase signal-to-noise ratio. (*D*) Molar ratios of H vs. GaO_2 (solid lines) and OH vs. GaO_2 (dashed lines) in IGO:PVA films from ToF-SIMS depth profiles. (*E*) ATR FT-IR of the IGO:PVA films; film thickness is increased to 20 nm to amplify the signal-to-noise ratio.

Moreover, PVA addition to 4 wt. % and 8 wt. % IGO:PVA weakens the O–H mode, with a gradual shift toward 3,450 cm^{-1} (4 wt. %) and 3,410 cm^{-1} (8 wt. %). Interestingly, additional PVA (12 wt. %) enhances the O–H mode again and shifts the peak to ~3,390 cm^{-1}. Note that the C–H stretch at ~2,900 cm^{-1} remains unchanged in all samples and that no H–O–H bending modes were detected near 1,635 cm^{-1}, excluding the possibility that the OH features are due to free or physiosorbed H_2O (43). Regarding Ga–H stretching modes expected near 2,000 cm^{-1} (44), careful analysis of the FT-IR data reveals no features in this range, indicating that the dominant form of H here must be –OH. The weakened O–H stretching intensity in the IGO:PVA films with 4 wt. % and 8 wt. % PVA indicates a lower oxide matrix –OH content, while the shift to lower frequencies is consistent with enhanced O–H covalency and/or O–H⋯O bond formation (45, 46). Thus, the ToF-SIMS and FT-IR data together indicate the presence of H, largely in the form of –OH in IGO, the composition of which falls in the 4 to 8 wt. % PVA incorporation range. Moreover, greater O–H covalency and/or increased H-bonding is detected on PVA incorporation.

High-Resolution Solid-State NMR Spectroscopic Analysis. To further examine the H chemical environment, the ^{1}H magic-angle spinning (MAS) NMR spectra of four IGO:PVA powders with 0 wt. %, 4 wt. %, 8 wt. %, and 12 wt. % PVA (see *SI Appendix,* Table S10 and Fig. S18 for details) are shown in Fig. 4*A*. The most intense ^{1}H resonance centered at δ 5.4 parts per million (ppm) in pristine IGO (0 wt. % PVA) suggests a high –OH group density in the film, in accord with the aforementioned infrared (IR) and SIMS measurements. The broad Gaussian line-shape (full-width at half-maximum = 2.73 kHz) ^{1}H signal indicated diverse local ^{1}H environments in pristine IGO, in agreement with the low crystallinity in the GIXRD spectra (Fig. 1*B*). Upon increasing the PVA content from 0 to 8 wt. %, the ^{1}H linewidths are essentially unchanged, consistent with the

amorphous character of IGO:PVA films. However, the broad ^{1}H peak slightly shifts from δ 5.4 ppm (0 wt. % PVA) to δ 5.1 ppm (4 wt. % PVA) to δ 4.8 ppm (8 wt. % PVA), and to δ 4.6 ppm (12 wt. % PVA). The slight shift is likely due to decreased –OH group acidity in the M–OH units, indicating greater O–H covalency, in accord with the FT-IR spectra (Fig. 3*E*), implying weaker O⋯H bonding in the IGO:PVA films with increasing PVA content. Surface OH^- groups (δ ~1 ppm) (47) were also detected in all four samples.

Next, one-dimensional ^{71}Ga MAS NMR spectra of 0 wt. %, 4 wt. %, 8 wt. %, and 12 wt. % IGO:PVA powders were acquired and are shown in Fig. 4*B* and *SI Appendix,* Fig. S19 and Table S11. In accord with the EXAFS data (Fig. 3*B*), ^{71}Ga MAS NMR reveals that the majority (>85%) of Ga sites are four-coordinate (Ga_{IV}) (48). As the PVA content increased, the six-coordinate Ga (Ga_{VI}) fraction gradually falls from 13.8% (pristine IGO) to 5.2% (4 wt. % PVA) to 1.3% (8 wt. % PVA), and to 0% (12 wt. % PVA) (*SI Appendix,* Table S11). The extremely large nuclear quadrupolar coupling constant, C_Q, in all of the four samples indicates that Ga, especially Ga_{IV}, is in a severely distorted low-symmetry local environment. Fig. 4*C* shows rotational-echo double-resonance (REDOR) experiments on IGO:PVA powders. REDOR NMR acquired the reference signal S_0 (without dephasing pulses) and the dephased signal S (with dephasing pulses–180° pulses on ^{1}H) under rotor synchronization. The signal difference, $\Delta S = S_0 - S$, suggests the extent to which the observed ^{71}Ga coherence was dephased due to ^{71}Ga–^{1}H spin-dipolar coupling interactions. The heteronuclear dipolar coupling constant extracted from REDOR measurements, d_{ij}, is strongly distance-dependent: $d_{ij} \propto 1/r_{ij}^3$, where r_{ij} is the distance between spins i and j. Therefore, the shorter the ^{71}Ga–^{1}H spin distance, the stronger the dipolar coupling, and, thus, the greater the magnetization magnitude dephasing in the observed ^{71}Ga coherence, i.e., the attenuated ^{71}Ga {^{1}H} REDOR signals. Information on ^{71}Ga–^{1}H spatial proximity can therefore be
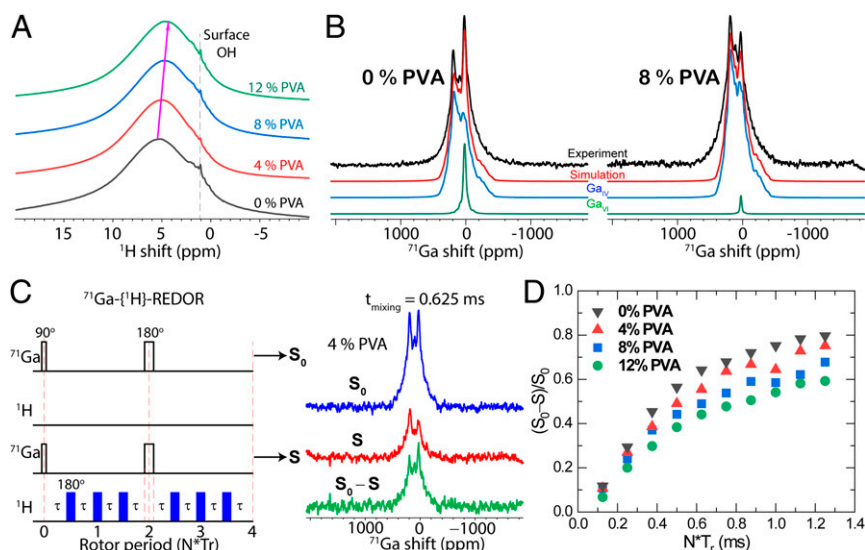
Fig. 4. NMR spectroscopy of IGO:PVA powders as a function of PVA content. (*A*) The ^{1}H MAS NMR spectra. (*B*) The ^{71}Ga MAS NMR spectra. (*C*) Schematic of the REDOR pulse sequence and an example of the ^{71}Ga NMR spectra without dephasing (S_0) and with dephasing (S), along with the difference ($\Delta S = S_0 - S$) after a mixing time of 0.625 ms. (*D*) The ^{71}Ga{^{1}H} REDOR curves.

obtained from the normalized $\Delta S/S_0$ as a function of dipolar coupling time. As shown in Fig. 4*D*, the build-up rate of the ^{71}Ga signal, $\Delta S/S_0$, decreased with higher PVA content. Considering the OH group O···H affinity suggested by the δ 5.4- to 4.6-ppm chemical shifts and the change in the broad ^{1}H peak intensity, the more rapid build-up of $\Delta S/S_0$ in the 0 wt. % PVA-based IGO:PVA powder is expected. As the PVA content increases, the −OH in IGO:PVA powders lead to slower ^{71}Ga dephasing by ^{1}H. As shown in Fig. 4*D*, $\Delta S/S_0$ decreases from 0.56 (0 wt. % PVA), to 0.49 (4 wt. % PVA), to 0.44 (8 wt. % PVA), and to 0.38 (12 wt. % PVA) at a 0.5-ms dipolar decoupling time (N^*T_r). The slower $\Delta S/S_0$ build-up in the IGO:PVA powders indicates ineffective dephasing of ^{71}Ga magnetization. As seen in the ^{1}H MAS (Fig. 4*A*) and IR (Fig. 3*E*) spectra, the O–H bonding in the IGO:PVA powders interferes with the dephasing process, while retaining higher S. Second-moment (M2) REDOR data analysis within the $\Delta S/S_0 < 0.3$ range yields average H–Ga distances (*SI Appendix*, Fig. S20), which increase from 3.23 ± 0.33 Å (0 wt. % PVA), to 3.30 ± 0.33 Å (4 wt. % PVA), to 3.36 ± 0.34 Å (8 wt. % PVA), and to 3.70 ± 0.37 Å (12 wt. % PVA). Note that the REDOR build-up curve suggests a distribution of Ga–H distances.

Next, ^{115}In MAS NMR spectra of 0 wt. %, 4 wt. %, 8 wt. %, and 12 wt. % IGO:PVA powders were acquired and are shown in *SI Appendix*, Fig. S21. The ^{115}In is a quadrupolar nucleus with spin 9/2 and has a large quadrupole moment Q of 77.0 fm^2 (49). Owing to large Q, the quadrupole interactions dominate, resulting in a very broad linewidth of >1 MHz, which introduces challenges in acquiring the full spectral range (50). The ^{115}In NMR spectra are therefore displayed by overlaying each individual spectrum collected at evenly spaced resonant-frequency intervals of ±144 kHz. The resulting broad ^{115}In resonances in all samples indicate similar In chemical environments in all of the IGO:PVA powders, in accord with the EXAFS results. By careful analysis of the spectra, the line-shape of ^{115}In signal in the central transition is seen to slightly narrow upon PVA addition, implicating a falling In quadruple coupling constant (C_Q) and, hence, a somewhat more uniform In environment. However, the line-shape deviates from a typical quadrupolar pattern (51) due to disordered In environments, which introduces challenges in spectral simulation to determine the exact magnitude of C_Q (51).

Theoretical Analysis of IGO H Doping. Based on the above experimental results, theoretical analyses were performed to further elucidate H-doping effects in amorphous oxides and in IGO in particular. Amorphous $In_{32}Ga_{22}O_{80}$ and $In_{32}Ga_{22}O_{79}$ were prepared via ab initio MD liquid-quench simulations and then doped with a single interstitial H radical (see *SI Appendix* for details of this approach). First, it was found that the most energetically favorable configurations in both $In_{32}Ga_{22}O_{80}H_1$ and $In_{32}Ga_{22}O_{79}H_1$ corresponded to M–OH unit formation with ~1.0 Å O–H bond lengths (Fig. 5*A*). This represents a strong covalent OH$^-$ bond, confirmed by a Bader-charge transfer analysis (Fig. 5*A*) and by the reduced O coordination number associated with weaker M–OH bonds (*SI Appendix*). Among the 40 cases with various H locations in IGO considered here, the higher-energy (less-favorable) configurations correspond to formation of interstitial H, where the H radical gains an additional electron from neighboring metals to become H$^-$, indicated by the calculated charge transfer (Fig. 5*B*). The calculated formation energy (*SI Appendix*) suggests that at 300 K, concentration of H interstitials is ~7 orders of magnitude lower than that of OH$^-$ in IGO$_{2.96}$.

To probe H-defect thermal stability and possible H mobility in a-IGO at 300 K, MD simulations were performed at 300 K for $In_{32}Ga_{22}O_{80}H_1$ and $In_{32}Ga_{22}O_{79}H_1$ (*SI Appendix*, Figs. S23–S25) by using the most energetically stable DFT configuration as the initial structure in each case (e.g., Fig. 5*A*). The MD simulations were run for ~250 ps (i.e., 124,000 ab initio MD steps) for each structure, after which the position of H and the time spent bonded to a specific O or as an interstitial in the vicinity of a metal atom were determined and are plotted in Fig. 5*C* ($In_{32}Ga_{22}O_{80}H_1$) and Fig. 5*D* ($In_{32}Ga_{22}O_{79}H_1$). Clearly, the H behavior at 300 K differs significantly in the two structures, having different O stoichiometries and different amounts of four-coordinate Ga (see *SI Appendix*, Figs. S22–S25 for details). The facile diffusion of H in $In_{32}Ga_{22}O_{80}H_1$ is the result of large fluctuations in the neighboring M–O bonds that make the potential wells rather shallow and increase the H probability to travel through the disordered structure. While in $In_{32}Ga_{22}O_{79}H_1$, H spent more than 11 times longer (115 ps) bonded to the O atom with the lowest effective coordination number when 300 K MD simulations were initiated using the most stable 0 K DFT position in $In_{32}Ga_{22}O_{79}H_1$
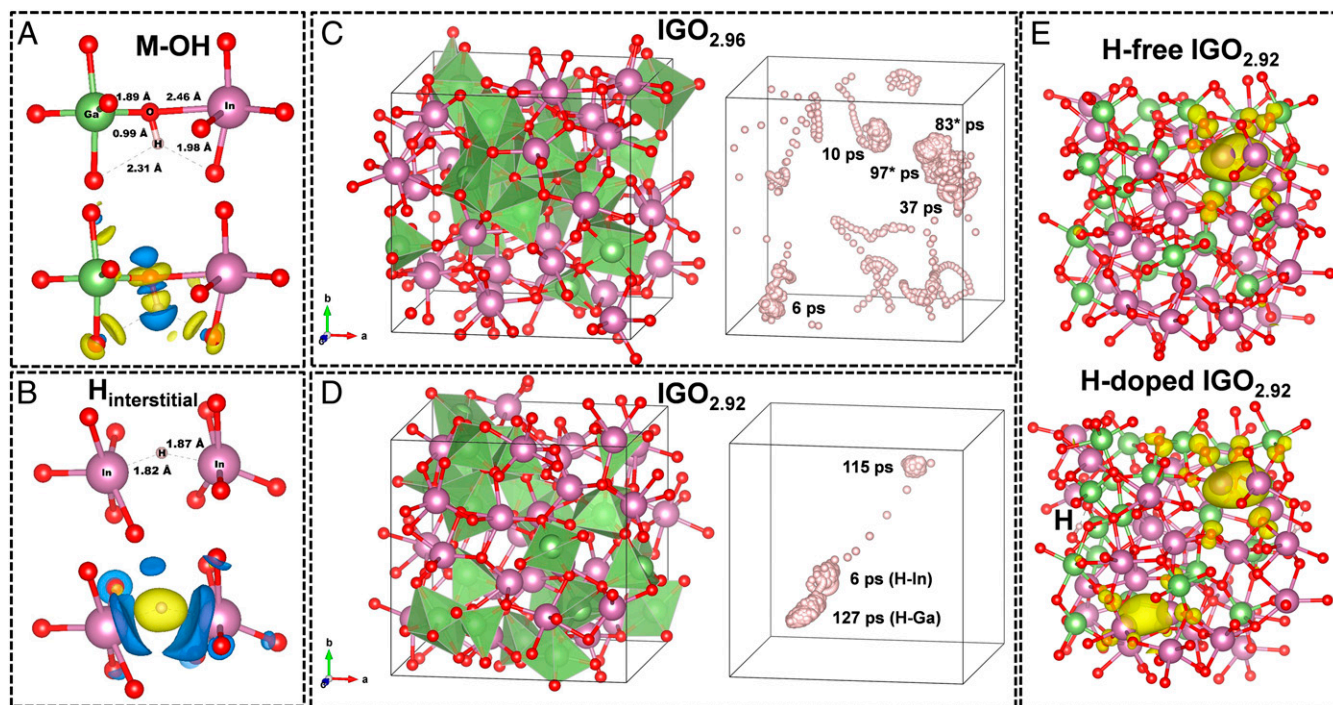
Fig. 5. Computed energetics of IGO H doping. (*A* and *B*) Calculated most energetically stable OH bond (*A*) and H interstitial (*B*) in $In_{32}Ga_{22}O_{80}H_1$. In each case, the calculated Bader charge transfer is shown as positive (yellow) and negative (blue) charge-density differences. (*C* and *D*) Structure of amorphous $In_{32}Ga_{22}O_{80}$ (IGO$_{2.96}$) (*C*) and $In_{32}Ga_{22}O_{79}$ (IGO$_{2.92}$) (*D*) with Ga polyhedra highlighted (green). Small red spheres represent O atoms, and large purple spheres represent In atoms. The position of H within the corresponding structure and the time the H spends bonded to an O atom are shown, with the exception of the two H-metal bonds labeled in parentheses. *Represents the case where H switches between two neighboring O atoms. (*E*) Calculated charge density distribution for deep trap defects in H-free and H-doped $In_{32}Ga_{22}O_{79}$.

(Fig. 5*D* and *SI Appendix*, Fig. S25*A*). The above results clearly suggest that highly distorted, undercoordinated atoms attract H, and the time during which the H remains bonded to an O or trapped between M atoms depends not only on the bond strength between the atom(s) and their other nearest neighbors, but also on the local structural dynamics. Moreover, in agreement with the present FT-IR and SS-NMR results, which give no evidence for Ga–H bonds, and that the calculated average Ga···H distance is >3.2 Å, the M–H distance distributions calculated from ab initio MD at 300 K (*SI Appendix*, Fig. S26) suggest that for $In_{32}Ga_{22}O_{80}$, the M-H distances are within 2.5 to 3.2 Å. This corresponds to an M–OH with the H attached to an O that is, in turn, bonded to Ga or In. For lower oxygen content, $In_{32}Ga_{22}O_{79}$, there are shorter-distance contributions that correspond to M–H–M defects, which is consistent with our total-energy DFT-Perdew–Burke–Ernzerhof (DFT-PBE) calculations at 0 K (Fig. 5*B*).

To understand the role of H in carrier generation and transport, the Heyd–Scuseria–Ernzerhof (HSE)-calculated electronic and optical properties of H-doped and H-free a-IGO (*SI Appendix*, Fig. S27) were also compared. Note that previous reports have suggested that the mobility in IGO is limited by the highly localized states near the Fermi level associated with Ga–O–Ga (22). Here, Bader charge contributions to the conduction states from all metal atoms were calculated before and after H-doping. The nearest metal neighbors in M–OH are found to give significantly higher contributions to the conduction states, namely, 1.2 to 1.4 times higher in $In_{32}Ga_{22}O_{80}H_1$ and 2.5 to 6.3 times higher in $In_{32}Ga_{22}O_{79}H_1$ vs. the H-free structures. Indeed, the calculated inverse participation ratio (IPR) shows that the states near the Fermi level are significantly more delocalized (lower IPR value) upon H doping. Accordingly, the low-energy absorption peak shifts from 0.8 to 0.5 eV (*SI Appendix*, Fig. S27).

The reason for the more uniform conduction charge density is a better hybridization due to weakening of the strongest Ga–O bonds and the resulting decreased distortions in all MO polyhedrals with attached OH⁻. The observed vigorous H diffusion at room temperature (Fig. 5*C*) is expected to facilitate the carrier-transport enhancement in the material since H spends enough time bonded to each O to optimize the local structure in its vicinity.

Furthermore, the presence of H reduces the localization of deep electron traps (*SI Appendix*, Fig. S27). In Fig. 5*E*, the calculated charge-density distributions for the deep trap defects in H-free and H-doped $In_{32}Ga_{22}O_{79}$ are shown. Before H doping, the trapped electron was localized between two undercoordinated, undershared In atoms, located at 2.82 Å from each other. Upon OH⁻ formation, the trapped charge density was found at two separate locations, the initial In–In pair (now at 2.78 Å) and a new one, with the In–In distance of 2.72 Å, which is significantly shorter compared to the 3.30 Å for these atoms in the H-free structure. The reason for the second short-distant In–In pair to form is a reduction of the In coordination from 4.33 and 4.90 to 3.81 and 3.97 upon the OH formation (*SI Appendix*). Integration of the charge distribution reveals that each area with localized charge contains only ∼0.5 e^-, suggesting an equal probability to find the electron in either of the two locations. Indeed, the localization of the deep defect decreases by almost one-half, as compared to the H-free case (*SI Appendix*, Fig. S27). This finding along with more uniform charge density within the conduction band agrees with the results from the optical and UPS data (*SI Appendix*, Table S7), where an E_F up-shift was observed with PVA incorporation, and explains the greater electron mobility in IGO:PVA.

Role of Ga and PVA in H Doping. To further understand the combined role of Ga and PVA in the H-doping process and the resulting TFT charge transport, a series of additional MO matrices having different metal compositions or different organic additives (polyvinyl phenol [PVP] and glycerol [Gly]) were investigated to replace PVA (Fig. 6 and *SI Appendix*, Figs. S28–S39). Previously, we reported that PVA suppresses charge transport in In_2O_3:PVA TFTs from ~4 cm^2/Vs (pristine In_2O_3) to ~0.6 cm^2/Vs with 6 wt. % PVA in the MO precursor solution (Fig. 6*A* and *SI Appendix*, Fig. S28) (52). Here, IZO:PVA and IGZO:PVA films were also fabricated to further probe the mechanism of PVA incorporation in IGO (*SI Appendix*, Fig. S29). As shown in Fig. 6*B*, in IZO:PVA (In:Zn = 7:3) TFTs, electron mobility monotonously falls as the PVA content increases from 0 to 10 wt. %, along with positively shifted V_T. Based on the XPS analysis of IGO:PVA and IZO:PVA films, it is clear that, in IGO:PVA films, high M–O–M content (>70%) is retained, even with 10 wt. % PVA (Fig. 1*C*). While in IZO, upon the addition of PVA, even though the remaining carbon content is similar (*SI Appendix*, Fig. S32), the M–O–M content drops considerably <70% (*SI Appendix*, Fig. S31), which will definitely erode electron transport. These data indicate that PVA-addition effects in MO systems without Ga can be quite different. Thus, to further probe the impact of different cations on PVA introduction, IGZO:PVA films with two different metal compositions (In:Ga:Zn = 72.5:7.5:20 and 1:1:1) were fabricated and characterized in TFT geometries (*SI Appendix*, Figs. S33 and S34). As shown in Fig. 6 *C* and *D*, while the mobility of IGZO(72.5:7.5:20) TFTs always decreases with increasing PVA content, for IGZO(1:1:1), the mobility first increases steeply from less than 10^{-3} cm^2/Vs (0 wt. % PVA) to ~0.1 cm^2/Vs (4 wt. % ~8 wt. % PVA) and only then decreases. It is obvious that for the IGZO with less Ga (IGZO with In:Ga:Zn = 72.5:7.5:20), PVA does not promote carrier mobility and only enlarges V_T (Fig. 6*C*), in contrast to the Ga-rich (In:Ga:Zn = 1:1:1) composition in which the mobility increases and V_T is reduced (Fig. 6*D*). Thus, it is found that for solution-processed Ga-free and Ga-poor MOs, PVA is ineffective in enhancing charge transport vs. PVP, which depresses the electron mobility (27).

Note also that, compared with our previous work on other MO-polymer systems such as using polyethyleneimine (PEI) and PVP (52, 53), PVA contrasts in two important respects: 1) No electron-rich electron-donor groups (e.g., amine in PEI) are present; and 2) compared to PVP, PVA cleanly decomposes during the fabrication process. Furthermore, since IGO:PVP films always yield inferior TFT performance (Fig. 6*E* and *SI Appendix*, Figs. S35 and S36; see *SI Appendix* for detailed discussion), it is clear that realization of high-performance, Ga-rich MO oxide semiconductors requires the use of a thermally labile polymer. Therefore, Gly (a small polyol molecule) was next investigated to replace PVA as a dopant since it shares similar chemical structures with large densities of –OH functional groups and Gly decomposes more easily compared to PVA (infra versa; *SI Appendix*, Fig. S39). As shown in *SI Appendix*, Fig. S37, similar to IGO:PVA, a very large increase in I_{ON} is obtained along with reduced hysteresis when Gly is added to the precursor. The TFT mobility and V_T (Fig. 6*F*) also indicate that Gly incorporation enhances device performance. Moreover, since Gly is a small molecule with functional groups (–OH) similar to those of PVA, it should act similarly to PVA and leave less residue in the resulting IGO films. Nevertheless, for PVA incorporation, a champion mobility of >7 cm^2/Vs is obtained, which is seven times higher than that with Gly incorporation (~1 cm^2/Vs). We suspect that the exceptionally high mobility for low-temperature solution-processed IGO (In:Ga = 6:4) films with PVA incorporation is due to the following factors. As shown in the thermogravimetric analysis plots of *SI Appendix*, Fig. S39, the PVA thermolysis process is very different from that of Gly,

with the latter compound being completely decomposed/vaporized below 200 °C, while PVA begins decomposition at ~250 °C, with the majority of the weight loss only occurring at ~300 °C. Note, however that PVA decomposition is far more efficient than that of PVP, where large amounts of PVP remain in the oxide film. As a result, the relatively slow decomposition speed of PVA may facilitate H diffusion to energetically stable sites in IGO, since the majority of the H in the films originate from the annealing atmosphere (*SI Appendix*, Fig. S16).

The present results, combined with the SS-NMR analysis and theoretical calculations, demonstrate that Ga in oxide semiconductors acts not only as an "oxygen getter," due to large MO lattice-formation enthalpy (13), but also can readily change coordination number from six to four, particularly in the presence of PVA (*SI Appendix*, Table S11). These Ga coordinative transformations enable structural adjustments that help preserve the M–O–M network after PVA addition—in contrast to IZO, where Zn invariably remains four-coordinate (22, 54, 55). Moreover, Zn always corner-shares with neighboring polyhedra, whereas Ga prefers edge-sharing (55), which may help suppress void formation and maintain lattice density. Additionally, low-coordinate Ga, promoted by PVA incorporation, effectively increases the low-coordinated O content (*SI Appendix*, Fig. S22) that attracts H and enhances the electrical properties discussed above. Thus, PVA thermolysis facilitates the Ga six- to four-coordinate transition and places H at energetically adventitious sites. In addition, the H in such IGO:PVA films decreases the local distortion of all neighboring polyhedra, increases free carrier transport by providing more uniform conduction charge density, and also suppresses the localization of deep electron traps.

Conclusions

Semiconducting IGO:PVA films (In:Ga = 6:4, atomic ratio) can be grown by a low-temperature-solution process. At optimal PVA content, the mobility of IGO:PVA TFTs is enhanced from 0.10 cm^2/Vs (neat IGO) to >7 cm^2/Vs (8 wt. % PVA)—among the highest mobilities reported for solution-processed IGO films. Analysis of film microstructure, composition, and electronic structure, combined with MD/DFT simulations, attributes the PVA-enhanced TFT performance to H doping of IGO with the
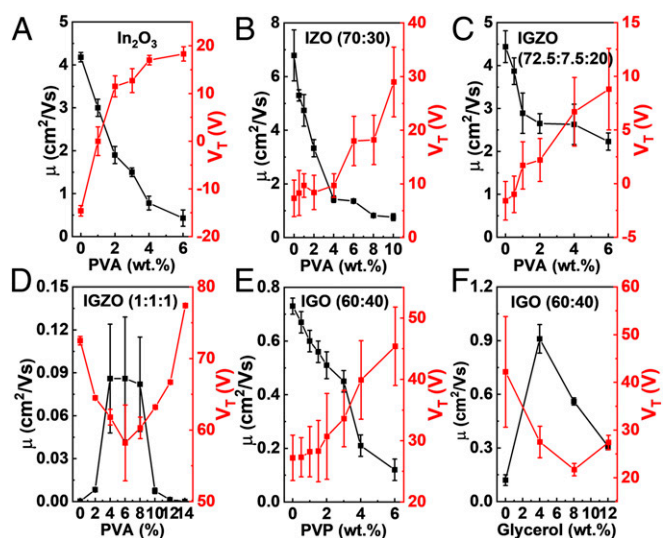
Fig. 6. Calculated mobility and V_T for TFTs of other MO systems. (*A*–*D*) In_2O_3 (*A*), IZO (*B*), IGZO (72.5:7.5:20) (*C*), and IGZO (1:1:1) (*D*) TFTs with different PVA content. (*E* and *F*) Calculated mobility and V_T of IGO (60:40) with PVP incorporation wt. % using 2-ME as solvent (*E*) and IGO (60:40) with Gly incorporation using water as solvent (*F*).

formation of OH groups, but not Ga–H bonds. Optimal amounts of H in IGO:PVA-derived films effectively suppress localized trap-site formation, reduce distortion of the metal coordination polyhedra, and afford far higher electron mobilities. Since achieving useful mobilities from solution-processed MO films with relatively high Ga content has presented a major scientific and technological challenge, the present approach circumvents the need to minimize Ga content and should be applicable to broad ranges of oxide electronics technologies.

Materials and Methods

Precursor Preparation. All chemicals were purchased from Sigma-Aldrich.* Exactly 354.8 mg of $In(NO_3)_3 \cdot xH_2O$, 297.2 mg of $Zn(NO_3)_2 \cdot xH_2O$, and 399.6 mg of $Ga(NO_3)_3 \cdot xH_2O$ were dissolved in 10-mL portions of DI water. After complete metal nitrate dissolution, the solutions were mixed to obtain the desired In/Ga, In/Zn, or In/Zn/Ga molar ratios. PVA (average $M_w = 13,000$ to 23,000, 98% hydrolyzed) was dissolved in DI water to a concentration of 8 mg/mL. Then, appropriate quantities of PVA solutions were added to the IGO precursor solutions to yield polymer:MO compositions from 0 to 14% by mass.

Device Fabrication and Measurements. For TFTs, n^{++} Si wafers with 300 nm of SiO_2 were used as gate electrodes and dielectrics, respectively. The Si wafer was first ultrasonically cleaned in an isopropyl alcohol bath for 20 min and then in an O plasma for 5 min. Then, the MO–polymer blend precursor was spin-coated on the Si/SiO2 wafers at 3,000 rpm for 20 s and annealed at 300 °C for 30 min. This IGO:PVA spin-coating and annealing process was repeated thrice to achieve a film thickness of ~10 nm. Finally, 40-nm Al source-drain electrodes with a channel length (L) of 100 μm and channel width (W) of 1 mm were thermally evaporated at 5×10^{-4} Pa. TFT electrical characterization utilized an Agilent B1500A semiconductor parameter analyzer under ambient. The field-effect mobility (μ) in saturation was calculated by using,

$$I_D = \frac{WC_i}{2L}\mu(V_{GS} - V_T)^2,\qquad [1]$$

where I_D is drain current, V_{GS} is the gate voltage, V_T is the threshold voltage, and C_i the capacitance per unit area.

IGO:PVA Film and Powder Characterization. AFM was conducted with a Veeco Dimension Icon Scanning Probe Microscope in tapping mode. GIXRD and XRR data were acquired with a Rigaku SmartLab Thin-Film Diffraction Workstation using a 9-kW Cu rotating anode source coupled to a multilayer optic. XPS was performed on Thermo Scientific ESCALAB 250Xi at a base pressure of 2×10^{-9} mBar. Spectra were obtained after etching the film surface for ~2 nm to minimize surface contamination. UPS spectra were also recorded on Thermo Scientific ESCALAB 250Xi at a base pressure of 2×10^{-8} mBar, using the He I line at hν = 21.21 eV with samples biased at −5 V. All UPS films were fabricated on indium tin oxide glass. EXAFS experiments were conducted at the 5BM-D beamline at the Advanced Photon Source of Argonne National Laboratory. Ultraviolet-visible (UV-vis) spectra were acquired with a Perkin-Elmer LAMBDA 1050 instrument. For EXAFS and UV-vis measurements, all films were fabricated on quartz substrates. ToF-SIMS depth profiling was accomplished with a PHI TRIFT III instrument with Ar^+ etching on films grown on a conducting Si wafer to avoid charging effects. FT-IR spectra were collected with a Thermo Nicolet Nexus 870 spectrometer having a single-reflection horizontal ATR accessory with a diamond ATR crystal fixed at a 45°incident angle. R-SoXS samples were prepared by using transparent Si_3N_4 windows (Silson) as substrates, following the same spin-coating and annealing process (300 °C) to coat IGO:PVA films. The two-dimensional R-SoXS data at different energies across the carbon K-edge were collected

at beamline 11.0.1.2[22] at the Advanced Light Source by using a Peltier-cooled (−45 °C) in vacuum (base pressure ~10^{-9} kPa [10^{-8} mBar]) and charge-coupled device detector (PI-MTE, Princeton Instruments; 2,048 × 2,048 pixels). The ^1H MAS SS-NMR experiments were performed on a Bruker Avance-III 500 spectrometer with a 2.5-mm HXY probe spinning at 25 kHz. All ^1H MAS NMR spectra were acquired by using a spin-echo pulse sequence with a 90° pulse length of 2.7 μs and a recycle delay of 15 s. The background signals were collected under identical conditions with the empty rotor and were subtracted from the experimental data. The ^1H chemical shift was calibrated with adamantane at δ 1.8 ppm. To investigate the spatial proximity of Ga and H, $^{71}Ga\{^1H\}$ REDOR NMR was carried out on IGO:PVA powders. All $^{71}Ga\{^1H\}$ REDOR experiments were performed on a Bruker 830 NEO spectrometer at the ^{71}Ga Larmor frequency of 253 MHz, spinning at 16 kHz using a home-built 3.2-mm probe. The 90° pulse lengths of 2 and 4 μs were employed for ^{71}Ga and ^1H, respectively. The ^{71}Ga chemical shift was calibrated with $Ga(NO_3)_{3(aq)}$ at δ 0.0 ppm. The ^{115}In MAS NMR spectra were collected by using a 3.2-mm home-built probe on a Bruker 830 NEO spectrometer operating at a Larmor frequency of 182.2 MHz. A frequency-stepped rotor-synchronized Quadrupolar Carr–Purcell–Meiboom–Gill pulse program was employed for acquisition at spinning rate of 16 kHz, with a 90° pulse length of 0.85 μs and recycle delay of 0.1 s to acquire the spectra. The resonant frequency was set at ±144-kHz intervals to excite the entire range. Crystalline indium oxide was used as calibration standard at δ 0.0 ppm. All NMR experiments were conducted at the National High Magnetic Field Laboratory.

Theoretical Computations. The amorphous $In_{32}Ga_{22}O_{80}$ and $In_{32}Ga_{22}O_{79}$ structures (In:Ga ~ 6:4 mol ratio) were obtained by using the ab initio MD liquid-quench approach, as implemented in the Vienna Ab Initio Simulation Package. The calculations were based on DFT with periodic boundary conditions and employed the PBE functional within the projector augmented-wave method. For an accurate structural analysis of the simulated amorphous oxides, 300 K In–Ga–O structures were used. The electronic and optical properties of the DFT-optimized amorphous H-free and H-doped In–Ga–O structures were calculated by using the hybrid HSE approach with a mixing parameter of 0.25 and a screening parameter α of 0.2 $Å^{-1}$. Detailed discussion of the ab initio MD simulations and DFT calculations can be found in *SI Appendix*.

Data Availability. All data are available in the main text and *SI Appendix*.

---

*Certain commercial equipment, instruments, or materials are identified in this paper in order to specify the experimental procedure adequately. Such identification is not intended to imply recommendation or endorsement by the National Institute of Standards and Technology, nor is it intended to imply that the materials or equipment identified are necessarily the best available for the purpose.

1. W. J. Scheideler, R. Kumar, A. R. Zeumault, V. Subramanian, Low-temperature-processed printed metal oxide transistors based on pure aqueous inks. *Adv. Funct. Mater.* **27**, 1606062 (2017).

2. X. Yu, T. J. Marks, A. Facchetti, Metal oxides for optoelectronic applications. *Nat. Mater.* **15**, 383–396 (2016).

3. J. Zhang *et al.*, Extremely high-gain source-gated transistors. *Proc. Natl. Acad. Sci. U.S.A.* **116**, 4843–4848 (2019).

4. R. Xu, J. He, W. Li, D. C. Paine, Performance enhancement of amorphous indium-zinc-oxide thin film transistors by microwave annealing. *Appl. Surf. Sci.* **357**, 1915–1919 (2015).

5. L. Petti *et al.*, Metal oxide semiconductor thin-film transistors for flexible electronics. *Appl. Phys. Rev.* **3**, 21303 (2016).

6. A. Liu *et al.*, Draw spinning of wafer-scale oxide fibers for electronic devices. *Adv. Electron. Mater.* **4**, 1700644 (2018).

7. Y.-H. Lin *et al.*, Hybrid organic–metal oxide multilayer channel transistors with high operational stability. *Nat. Electron.* **2**, 587–595 (2019).

8. D. Louloudakis *et al.*, Novel spark method for deposition of metal oxide thin films: Deposition of hexagonal tungsten oxide. *Phys. Status Solidi., A Appl. Mater. Sci.* **216**, 1800513 (2019).

9. Q. Wang *et al.*, Effects of self-assembled monolayer modification of nickel oxide nanoparticles layer on the performance and application of inverted perovskite solar cells. *ChemSusChem* **10**, 3794–3803 (2017).

10. K. Nomura *et al.*, Room-temperature fabrication of transparent flexible thin-film transistors using amorphous oxide semiconductors. *Nature* **432**, 488–492 (2004).

11. V. Kampylafka *et al.*, Long-term stability of transparent n/p ZnO homojunctions grown by rf-sputtering at room-temperature. *J Materiomics* **5**, 428–435 (2019).

12. S. Park *et al.*, Sub-0.5 V highly stable aqueous salt gated metal oxide electronics. *Sci. Rep.* **5**, 13088 (2015).

13. J. W. Hennek *et al.*, Oxygen "getter" effects on microstructure and carrier transport in low temperature combustion-processed a-InXZnO (X = Ga, Sc, Y, La) transistors. *J. Am. Chem. Soc.* **135**, 10729–10741 (2013).

14. Y. Song *et al.*, Top-gated indium–zinc–oxide thin-film transistors with in situ Al2O3/HfO2 gate oxide. *IEEE Electron Device Lett.* **35**, 1251–1253 (2014).

15. S. L. Moffitt *et al.*, Probing the unique role of gallium in amorphous oxide semiconductors through structure-property relationships. *Adv. Electron. Mater.* **3**, 1700189 (2017).

16. J. S. Park, W. J. Maeng, H. S. Kim, J. S. Park, Review of recent developments in amorphous oxide semiconductor thin-film transistor devices. *Thin Solid Films* **520**, 1679–1693 (2012).

17. J. H. Yang, D. K. Kim, M. H. Yoon, G. H. Kim, S. M. Yoon, Mechanically robust and highly flexible nonvolatile charge-trap memory transistors using conducting-polymer electrodes and oxide semiconductors on ultrathin polyimide film substrates. *Adv. Mater. Technol.* **4**, 1900348 (2019).

18. K. K. Banger *et al.*, Low-temperature, high-performance solution-processed metal oxide thin-film transistors formed by a "sol–gel on chip" process. *Nat. Mater.* **10**, 45–50 (2011).

19. Y. H. Kim *et al.*, Flexible metal-oxide devices made by room-temperature photochemical activation of sol-gel films. *Nature* **489**, 128–132 (2012).

20. X. Liu *et al.*, A low-temperature, solution processable tin oxide electron-transporting layer prepared by the dual-fuel combustion method for efficient perovskite solar cells. *Adv. Mater. Interfaces* **3**, 1600122 (2016).

21. J. Socratous *et al.*, Electronic structure of low-temperature solution-processed amorphous metal oxide semiconductors for thin-film transistor applications. *Adv. Funct. Mater.* **25**, 1873–1885 (2015).

22. J. E. Medvedeva, D. B. Buchholz, R. P. H. Chang, Recent advances in understanding the structure and properties of amorphous oxide semiconductors. *Adv. Electron. Mater.* **3**, 1700082 (2017).

23. A. Liu *et al.*, Solution combustion synthesis: Low-temperature processing for p-type Cu:NiO thin films for transparent electronics. *Adv. Mater.* **29**, 1701599 (2017).

24. D. Khim *et al.*, Modulation-doped In2O3/ZnO heterojunction transistors processed from solution. *Adv. Mater.* **29**, 1605837 (2017).

25. J. H. Park *et al.*, Effect of acetic acid on the performance of solution-processed gallium doped indium oxide thin film transistors. *J. Sol-Gel Sci. Technol.* **67**, 130–134 (2013).

26. C. H. Choi, Y. W. Su, L. Y. Lin, C. C. Cheng, C. H. Chang, The effects of gallium on solution-derived indium oxide-based thin film transistors manufactured on display glass. *Rsc Adv.* **5**, 93779–93785 (2015).

27. X. Yu *et al.*, Ultra-flexible, "invisible" thin-film transistors enabled by amorphous metal oxide/polymer channel layer blends. *Adv. Mater.* **27**, 2390–2399 (2015).

28. B. Wang *et al.*, Carbohydrate-assisted combustion synthesis to realize high-performance oxide transistors. *J. Am. Chem. Soc.* **138**, 7067–7074 (2016).

29. Y. Hanyu *et al.*, Hydrogen passivation of electron trap in amorphous In-Ga-Zn-O thin-film transistors. *Appl. Phys. Lett.* **103**, 202114 (2013).

30. H. Tang *et al.*, Effects of residual hydrogen in sputtering atmosphere on structures and properties of amorphous In-Ga-Zn-O thin films. *J. Appl. Phys.* **118**, 205703 (2015).

31. L. Xu *et al.*, Rational hydrogenation for enhanced mobility and high reliability on ZnO-based thin film transistors: From simulation to experiment. *ACS Appl. Mater. Interfaces* **8**, 5408–5415 (2016).

32. J. J. Meléndez, M. Wierzbowska, In2O3 doped with hydrogen: Electronic structure and optical properties from the pseudopotential self-interaction corrected density functional theory and the random phase approximation. *J. Phys. Chem. C* **120**, 4007–4015 (2016).

33. C. Chen *et al.*, Analysis of ultrahigh apparent mobility in oxide field-effect transistors. *Adv. Sci.* **6**, 1801189 (2019).

34. M. H. Kim *et al.*, Photochemical hydrogen doping induced embedded two-dimensional metallic channel formation in InGaZnO at room temperature. *ACS Nano* **9**, 9964–9973 (2015).

35. K. Hayashi *et al.*, Photoelectron emission yield experiments on evolution of sub-gap states in amorphous In-Ga-Zn-O thin films with post deposition hydrogen treatment. *Appl. Phys. Lett.* **107**, 112104 (2015).

36. S. W. Tsao *et al.*, Hydrogen-induced improvements in electrical characteristics of a-IGZO thin-film transistors. *Solid-State Electron.* **54**, 1497–1499 (2010).

37. M. P. A. Jallorina, J. P. S. Bermundo, M. N. Fujii, Y. Ishikawa, Y. Uraoka, Significant mobility improvement of amorphous In-Ga-Zn-O thin-film transistors annealed in a low temperature wet ambient environment. *Appl. Phys. Lett.* **112**, 193501 (2018).

38. H. Tang *et al.*, Multiple roles of hydrogen treatments in amorphous in–Ga–Zn–O films. *ECS J. Solid State Sci. Technol.* **6**, 365-P372 (2017).

39. J. Kim *et al.*, A study on H2 plasma treatment effect on a-IGZO thin film transistor. *J. Mater. Res.* **27**, 2318–2325 (2012).

40. T. Kamiya, H. Hosono, Roles of hydrogen in amorphous oxide semiconductor. *ECS Trans.* **54**, 103–113 (2013).

41. S. Limpijumnong, P. Reunchan, A. Janotti, C. G. Van de Walle, Hydrogen doping in indium oxide: An ab initio study. *Phys. Rev. B Condens. Matter Mater. Phys.* **80**, 193202 (2009).

42. F. A. Stevie *et al.*, SIMS measurement of hydrogen and deuterium detection limits in silicon: Comparison of different SIMS instrumentation. *J. Vac. Sci. Technol. B* **34**, 03H103 (2016).

43. B. L. Mojet, S. D. Ebbesen, L. Lefferts, Light at the interface: The potential of attenuated total reflection infrared spectroscopy for understanding heterogeneous catalysis in water. *Chem. Soc. Rev.* **39**, 4643–4655 (2010).

44. W. Jochum *et al.*, Hydrogen on polycrystalline β-Ga2O3: Surface chemisorption, defect formation, and reactivity. *J. Catal.* **256**, 268–277 (2008).

45. A. A. Tsyganenko, V. N. Filimonov, Infrared-spectra of surface hydroxyl groups and crystalline-structure of oxides. *Spectrosc. Lett.* **5**, 477–487 (1972).

46. L. Benco, D. Tunega, J. Hafner, H. Lischka, Upper limit of the O–H···O hydrogen bond. Ab initio study of the kaolinite structure. *J. Phys. Chem. B* **105**, 10812–10817 (2001).

47. L. Gill *et al.*, Fast MAS 1H NMR study of water adsorption and dissociation on the (100) surface of ceria nanocubes: A fully hydroxylated, hydrophobic ceria surface. *J. Phys. Chem. C* **121**, 7450–7465 (2017).

48. D. Massiot *et al.*, 71Ga and 69Ga nuclear magnetic resonance study of β-Ga2O3: Resolution of four- and six-fold coordinated Ga sites in static conditions. *Solid State Nucl. Magn. Reson.* **4**, 241–248 (1995).

49. H. Hamaed *et al.*, A 115In solid-state NMR study of low oxidation-state indium complexes. *Chem. Sci.* **5**, 982–995 (2014).

50. S. E. Ashbrook, Recent advances in solid-state NMR spectroscopy of quadrupolar nuclei. *Phys. Chem. Chem. Phys.* **11**, 6892–6905 (2009).

51. R. E. Wasylishen, S. E. Ashbrook, S. Wimperis, *NMR of Quadrupolar Nuclei in Solid Materials*, (Wiley-VCH, Weinheim, Germany, 2012).

52. W. Huang *et al.*, Metal oxide transistors via polyethylenimine doping of the channel layer: Interplay of doping, microstructure, and charge transport. *Adv. Funct. Mater.* **26**, 6179–6187 (2016).

53. W. Huang *et al.*, Metal composition and polyethylenimine doping capacity effects on semiconducting metal oxide-polymer blend charge transport. *J. Am. Chem. Soc.* **140**, 5457–5473 (2018).

54. J. E. Medvedeva, R. Khanal, Long-range structural correlations in amorphous ternary In-based oxides. *Vacuum* **114**, 142–149 (2015).

55. R. Khanal, D. B. Buchholz, R. P. H. Chang, J. E. Medvedeva, Composition-dependent structural and transport properties of amorphous transparent conducting oxides. *Phys. Rev. B Condens. Matter Mater. Phys.* **91**, 205203 (2015).